

Electroconductive RGO-MXene membranes with wettability-regulated channels: improved water permeability and electro-enhanced rejection performance

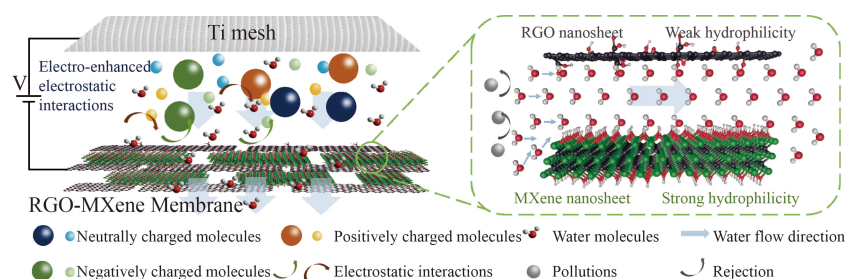
Xiaoying Wang, Haiguang Zhang, Xu Wang, Shuo Chen, Hongtao Yu, Xie Quan (✉)

Key Laboratory of Industrial Ecology and Environmental Engineering (Ministry of Education), School of Environmental Science and Technology, Dalian University of Technology, Dalian 116024, China

HIGHLIGHTS

- Electroconductive RGO-MXene membranes were fabricated.
- Wettable membrane channels were established between RGO and MXene nanosheets.
- Hydrophilic MXene reduces the resistance of water entering the membrane channels.
- Water permeance of RGO-MXene membrane is 16.8 times higher than that of RGO membrane.
- Electro-assistance can enhance the dye rejection performance of RGO-MXene membrane.

GRAPHIC ABSTRACT



ARTICLE INFO

Article history:

Received 22 March 2022

Revised 17 June 2022

Accepted 19 June 2022

Available online 20 July 2022

Keywords:

Reduced graphene oxide

MXene

Membrane

Water permeance

Dye rejection

Electro-assistance

ABSTRACT

Reduced graphene oxide (RGO) membranes are theoretically more conducive to the rapid transport of water molecules in their channels compared with graphene oxide (GO) membranes, as they have fewer oxygen-containing functional groups and more non-oxidized regions. However, the weak hydrophilicity of RGO membranes inhibits water entry into their channels, resulting in their low water permeability. In this work, we constructed wettable RGO-MXene channels by intercalating hydrophilic MXene nanosheets into the RGO membrane for improving the water permeance. The RGO-MXene composite membrane exhibits high pure water permeance of $62.1 \text{ L}/(\text{m}^2 \cdot \text{h} \cdot \text{bar})$, approximately 16.8 times that of the RGO membrane ($3.7 \text{ L}/(\text{m}^2 \cdot \text{h} \cdot \text{bar})$). Wettability test results and molecular dynamics simulations suggest that the improved water permeance results from the enhanced wettability of RGO-MXene membrane and increased rate of water molecules entering the RGO-MXene channels. Benefiting from good conductivity, the RGO-MXene membrane with electro-assistance exhibits significantly increased rejection rates for negatively charged dyes (from 56.0% at 0 V to 91.4% at 2.0 V for Orange G) without decreasing the permeate flux, which could be attributed to enhanced electrostatic repulsion under electro-assistance.

© Higher Education Press 2023

1 Introduction

Membrane separation technology has become one of the most effective methods for water treatment, owing to its advantages of high separation efficiency, convenient operation and low-energy consumption (Wei et al., 2019a; Wang et al., 2021). The membranes prepared from

graphene oxide (GO) have received extensive attention because of their excellent water permeability. However, the abundant oxygen-containing groups of GO membranes can lead to poor water-stability because of the swelling effect (Liu et al., 2021). Previous studies have shown that the high water permeability of GO membranes is attributable to rapid water transport in the atomically smooth sp^2 regions (non-oxidized regions) of their membrane channels (Abraham et al., 2017; Xu et al., 2017). Therefore, increasing the proportion of sp^2 region contributes to increasing

✉ Corresponding author

E-mail: quanxie@dlut.edu.cn

the water transport rate, while enhancing the stability of the membrane in water simultaneously. Compared to GO membranes, reduced GO (RGO) membranes show fewer oxygen-containing groups and higher proportion of non-oxidized regions in their channels (Fan et al., 2020). This implies that RGO membranes could theoretically allow faster water transport velocity than GO membranes (Willcox et al., 2017b). However, experimental results from literatures indicated that the RGO membranes generally show very low water permeabilities, even lower than $1.0 \text{ L}/(\text{m}^2 \cdot \text{h} \cdot \text{bar})$ (Su et al., 2014; Sun et al., 2019). The reduction process of GO to RGO can decrease the number of oxygen functional groups on RGO nanosheets, thus, RGO membranes exhibit weaker hydrophilicity and narrower interlayer spacing (Huang et al., 2018). Despite rapid transport of water molecules in the non-oxidized regions of RGO membrane channels, their weakly hydrophilic and narrow membrane channels could hamper the entry of water molecules into the channels (Lian et al., 2018), resulting in lower water permeability. In addition, the reduction of oxygen functional groups on the RGO membrane surface would weaken the electrostatic interactions between the membrane and charged species, which could lower the rejection rates for these charged species.

Xu et al. fabricated an RGO membrane and found that its water flux could be significantly improved from < 1.0 to $44.0 \text{ L}/(\text{m}^2 \cdot \text{h} \cdot \text{bar})$ after oxygen plasma etching (Xu et al., 2018). Sun et al. demonstrated that an RGO membrane modified with oxygen-containing groups (O-RGO membrane) had 2.6 times greater water flux than the untreated membrane (Sun et al., 2019). These studies suggest that hydrophilic regulation of membranes could improve of their water permeability. By modeling the transport of water molecules in Janus GO membrane, Liu et al. found that, compared with a membrane channel with pristine graphene surface on both sides, a channel with pristine graphene surface on one side and oxidized graphene surface on the other was more favorable for the rapid transport of water molecules (Willcox et al., 2017a; Liu et al., 2020). It is therefore inferred that intercalation of a hydrophilic, two-dimensional (2D) material into an RGO membrane could construct similar Janus nanochannels with RGO as the graphene region and hydrophilic material as the oxidized graphene region, which may decrease the energy barrier for water molecules entering membrane channels and enable ultrafast water transport in them (Abaie et al., 2021). MXene, a 2D material, possesses good hydrophilicity with a water contact angle of less than 30° (Li et al., 2019). If intercalated into an RGO membrane, the strong hydrophilicity of MXene could increase the affinity between water molecules and the entrance of membrane channels, thereby weakening the resistance of water molecules entering the membrane channels and increasing water flux. Moreover, the intrinsic conductivities of RGO and MXene could endow

MXene-intercalated RGO membrane good conductivity (Park et al., 2009; Sang et al., 2016). Therefore, the rejection performance could be further improved under electro-assistance through electro-adsorption, electrochemical degradation and electrostatic interactions (Yi et al., 2018; Wei et al., 2021).

In this work, electroconductive MXene-intercalated RGO (RGO-MXene) membranes with wettability-regulated channels are constructed by intercalating MXene into RGO membranes. It is hypothesized that hydrophilic MXene could lower the entry resistance of water molecules into the channels, thereby improving membrane permeance, and that electro-assistance could further increase the rejection ability toward charged molecules through electrostatic interactions. To validate this hypothesis, molecular dynamics simulations are employed to analyze the movements of water molecules into the channels of RGO and RGO-MXene membranes. Furthermore, the rejection performances of RGO-MXene membranes toward various dye molecules under electro-assistance are investigated. As a result, the RGO-MXene membrane shows higher hydrophilicity and surface charge than those of the RGO membrane. The intercalation of MXene increases the rate of water molecules entering the membrane channels, resulting in a 16.8-fold increase in water flux. Moreover, the enhanced electrostatic repulsion effectively improves the rejection rates of charged dyes by the RGO-MXene membranes under electro-assistance.

2 Materials and methods

2.1 Chemicals and materials

Pristine graphite powders (2000 mesh, AR) and lithium fluoride (LiF, purity 99%) were purchased from Aladdin Chemistry Co., Ltd., Shanghai, China. Ti_3AlC_2 powders (400 mesh, purity 98%) were purchased from 11 Technology Co., Ltd., Jilin, China. Hydrochloric acid (HCl, AR, 36%–38%) and sulfuric acid (H_2SO_4 , AR, 98%) were provided by Tianjin Kemio Chemical Reagent Development Center, Tianjin, China. Hydrogen peroxide (H_2O_2 , 30%), potassium permanganate (KMnO_4 , purity $\geq 99\%$), ammonia solution ($\text{NH}_3 \cdot \text{H}_2\text{O}$, 25%) and hydrazine hydrate ($\text{N}_2\text{H}_4 \cdot \text{H}_2\text{O}$, 80 wt.%) were supplied by Sinopharm Chemical Reagent Co., Ltd., China. Polyvinylidene fluoride (PVDF) membranes (pore size of $0.1 \mu\text{m}$ and diameter of 47 mm) were supplied by Merck Millichannel Co., Ltd., Shanghai, China. Rhodamine B (RhB, purity $\geq 95\%$), Alcian Blue (AB, purity $\geq 50\%$), Methyl Orange (MO, purity $> 96\%$), Congo Red (CR, purity $> 98\%$), Coomassie Brilliant Blue (CBB, AR) and Methyl Blue (MB, purity $> 99\%$) were purchased from Tianjin Damao Chemical Reagent Factory, Tianjin, China. Orange G (OG, purity $\geq 96\%$) and Methylene Blue (MLB, purity $\geq 98\%$) were purchased from Aladdin Chemistry Co., Ltd., Shanghai, China.

2.2 Preparation of RGO and MXene

Preparation of RGO. Firstly, the GO nanosheets were synthesized by exfoliating pristine graphite powders using a modified Hummers' method (Wei et al., 2020). Then, the prepared GO was ultrasonically dispersed to form a GO aqueous dispersion (0.05 mg/mL). Subsequently, $\text{NH}_3 \cdot \text{H}_2\text{O}$ (80 μL , 25% in water) and $\text{N}_2\text{H}_4 \cdot \text{H}_2\text{O}$ (12 μL , 80 wt.% in water) were added into the GO dispersion (30 mL), which were heated at 90 °C for 1.5 h to obtain RGO dispersion.

Preparation of MXene. In a typical procedure, 1.6 g LiF and 1.0 g Ti_3AlC_2 were slowly added into 20 mL HCl solution (9 mol/L) under stirring, and then the reaction was continued for 24 h in a 45 °C water bath (Pandey et al., 2020). After several times of centrifugal cleaning, $\text{Ti}_3\text{C}_2\text{T}_x$ dispersion with a pH value of about 6 was obtained. Then further ultrasonic exfoliating was carried out to prepare the MXene dispersion. The as-prepared dispersion was diluted to a concentration of 0.05 mg/mL and stored in a refrigerator at -4 °C under the protection of argon gas.

2.3 Fabrication of RGO and RGO-MXene membranes

Fabrication of RGO membrane. The dispersion (2 mL) of RGO was added to 20 mL of ultrapure water and then treated with ultrasonication for 10 min (Fig. S1). Then the RGO membrane was fabricated by vacuum-filtrating the prepared dispersion with PVDF membrane substrates.

Fabrication of RGO-MXene membranes. The mixtures (2 mL) of RGO and MXene dispersions were added to 20 mL of ultrapure water and then treated with ultrasonication for 10 min (Fig. 1(a)). Then the RGO-MXene membranes were fabricated by vacuum-filtrating the prepared mixtures with PVDF membrane substrates. By adjusting the ratio of MXene to RGO in the mixture, the RGO-MXene membranes with different MXene mass percentages of 30 wt.%, 50 wt.%, 60 wt.%, 65 wt.%, and 70 wt.% were obtained, which were respectively labeled as RM-30, RM-50, RM-60, RM-65 and RM-70 membranes.

2.4 Membrane characterizations

The microtopographies of the RGO nanosheets, MXene

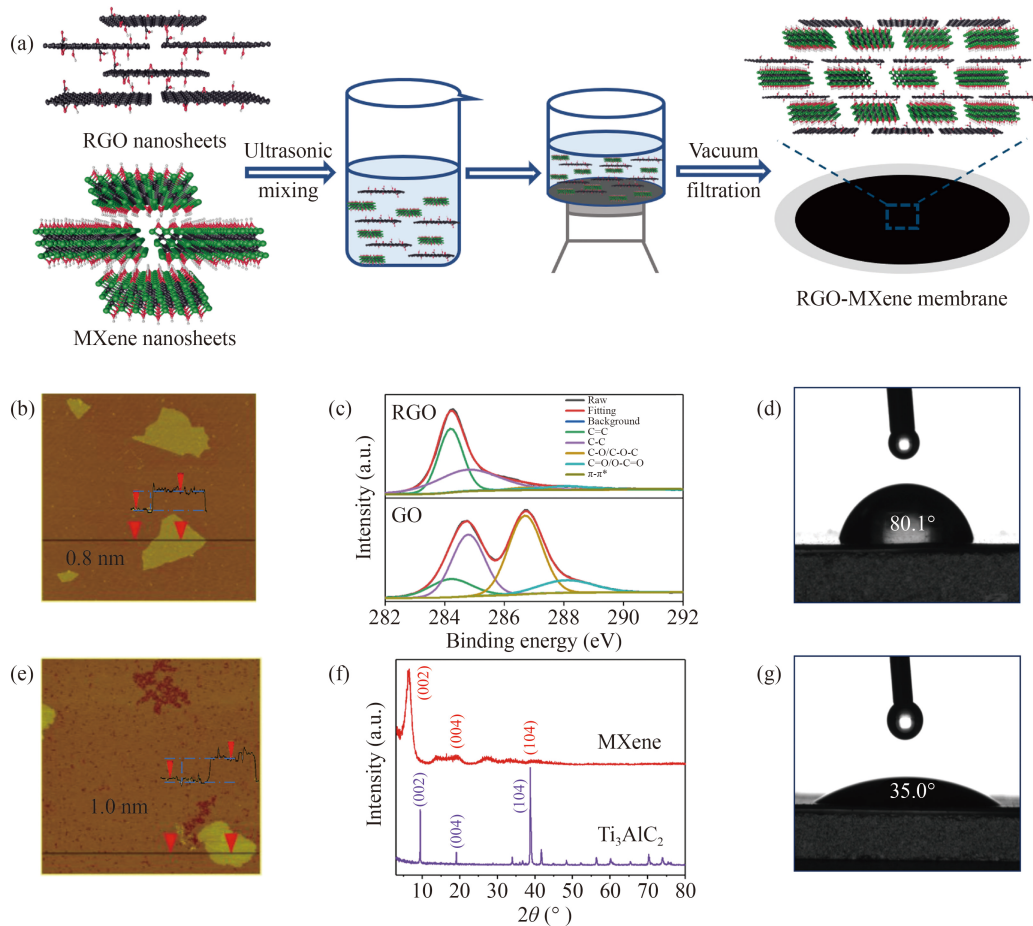


Fig. 1 (a) Illustration of the preparation process of RGO-MXene membranes; (b) AFM image of RGO nanosheets; (c) XPS C 1s spectra of RGO and GO; (d) Water contact angle of RGO; (e) AFM image of MXene nanosheets; (f) XRD spectra of MXene and Ti_3AlC_2 ; (g) Water contact angle of MXene.

nanosheets and RGO-MXene membranes were recorded by a scanning electron microscope (SEM, Hitachi S4800, Japan). The thicknesses of the RGO and MXene nanosheets were measured by an atomic force microscopy (AFM, Nanoscope IIIA+, Veeco, USA). The elemental composition and structures of GO, RGO, Ti_3AlC_2 , $\text{Ti}_3\text{C}_2\text{T}_x$ and RGO-MXene membranes were analyzed by X-ray photoelectron spectrometer (XPS, EscaLab 250 Xi, Waltham, MA, USA) and X-ray diffractometer (XRD, EMPYREAN, PANalytical, Netherlands). Raman spectrometer was applied to determine the molecular structures of the RGO-MXene membranes (Raman, DXR Microscope, Thermo Fisher Scientific Inc., USA). The element distribution of RGO-MXene membrane was measured by energy dispersive X-ray spectroscopy (EDS, JSM-7900F, JEOL, Japan). The contact angles of RGO-MXene membranes were measured by an optical contact angle meter (SL 200 KB, KINO, USA). The Zeta potentials of the RGO-MXene membranes were analyzed using a laser particle size and zeta potential analyzer (Zetasizer Nano ZS90, Malvern, Britain). The conductivities of RGO-MXene membranes were tested by a digital four-probe tester (ST2258c, Jingge Electronic Co., Ltd., Suzhou, China).

2.5 Membrane performance evaluations

The membrane performance was tested using a cross-flow filtration setup (Fig. S2). The effective area of the RGO-MXene membrane for filtration test was 8.04 cm^2 . In the filtration processes, the feed was pumped into the membrane module through a peristaltic pump, and the transmembrane pressure difference was controlled by a valve. During electro-assisted membrane processes, the RGO-MXene membrane also acted as a cathode, and a titanium (Ti) mesh was placed into the module as the anode. Voltages were applied between membrane cathode and titanium mesh anode by a DC power supply. Before the performance evaluations, the RGO-MXene membranes were pre-pressured with ultra-pure water with a conductivity of $18 \text{ M}\Omega \cdot \text{cm}$ for 2 h at a pressure of 1 bar.

Ultra-pure water was used to test the pure water permeance of the RGO-MXene membranes. Next, a series of dyes including neutrally charged dye RhB, positively charged dyes (MLB and AB) and negatively charged dyes (MO, CR, CBB and MB) at the concentration of 20 mg/L were employed for testing the membrane rejection performance. All tests were performed at a pressure difference of 1 bar. The water permeance (J_w , $\text{L}/(\text{m}^2 \cdot \text{h} \cdot \text{bar})$) and the dye rejection rate (R , %) were calculated following Eqs. (1) and (2), respectively.

$$J_w = \frac{\Delta m \times 10^{-3}}{\rho \times A \times 10^{-4} \times t \times \Delta p}, \quad (1)$$

where Δm (g) is the mass of permeated water; ρ (g/cm^3) is the density of water; A (cm^2) is the effective area of the membrane; t (h) is the operation time; Δp (bar) is the transmembrane pressure difference.

$$R = \frac{C_f - C_p}{C_f} \times 100\%, \quad (2)$$

where C_f (mg/L) is the concentration of the dye in the feed solution; C_p (mg/L) is the concentration of the dye in the permeate solution. The concentrations of the dyes were detected using a UV-visible absorption spectrometer (UV-2600, Shimadzu, Japan).

2.6 Molecular dynamics simulation

The molecular dynamics simulation was performed to investigate the movements of water molecules into two channels constructed by RGO-RGO and RGO-MXene nanosheets using the LAMMPS package (Fig. S3). The area of RGO nanosheet and MXene nanosheet was $36.9 \times 30.6 \text{ \AA}^2$. The width of both channels was 7 \AA . The total number of water molecules in the simulation box is 3860. In the simulation system, periodic boundary conditions (PBC) were applied to all dimensions. The all-atom optimized potentials for liquid simulations (OPLS-AA) and the extended simple point charge model (SPC/E) were applied for the simulations. The movements of water molecules entering into the two channels were observed, and the number of water molecules in the channels and the interaction energy between the water molecules and the channels were recorded. The detailed modeling and simulations parameters are shown in Table S1.

3 Results and discussion

3.1 Characterizations of RGO and MXene nanosheets

The AFM images (Figs. 1(b) and S4(a)) show that the thickness of the RGO nanosheet is about 0.8 nm , indicating that it has a single- or double-layered structure (Wei et al., 2019b). The SEM image further shows the 2D thin-layered structure of the RGO nanosheets (Fig. S4(b)). The XPS C 1s spectra (Fig. 1(c) and Table S2) show that the proportion of C=C bond significantly increases from $13.2 \text{ at.}\%$ for GO to $64.7 \text{ at.}\%$ for RGO, and the proportion of oxygen-containing groups decreases from $53.8 \text{ at.}\%$ to $12.7 \text{ at.}\%$, suggesting that more atomically smooth sp^2 regions are obtained. The XRD pattern of RGO (Fig. S4(c)) shows only one distinct characteristic peak at 23.4° , while the characteristic peak of GO is located at 11.1° . This result further indicates the reduction of GO to RGO. After reduction, the water contact angle increases from 37.6° for GO to 80.1° for RGO (Figs. 1(d) and S4(d)), demonstrating that the reduction process results in weak hydrophilicity of RGO.

The AFM results (Figs. 1(e) and S5(a)) show that the prepared MXene nanosheet has a thickness of about 1.0 nm , suggesting that it has a mono-layered structure (Ming et al., 2020). The SEM image shows a semi-transparent MXene nanosheet on an anodic aluminum oxide support

(Fig. S5(b)), implying that the MXene nanosheet has a thin layer structure, which is in agreement with the AFM results. To determine the removal of the Al layer, crystal structure and elemental composition analyses were performed on Ti_3AlC_2 and MXene. In the XRD pattern of MXene (Fig. 1(f)), the diffraction peak of Al at 39° (2θ , (104)) almost disappears. In comparison with the XRD patterns of MXene and Ti_3AlC_2 , a left shift of (002) peak from 9.6° to 6.3° (2θ) indicates that the interlayer spacing is increased. Furthermore, the broadening of (002) and (004) peaks further demonstrate the synthesis of MXene (Naguib et al., 2011). The water contact angle of MXene is 35.0° (Fig. 1(g)), which is significantly smaller than

that of RGO, indicating that the hydrophilicity of MXene is higher than that of RGO.

3.2 Characterization of RGO-MXene membranes

The SEM image of the RGO membrane (Fig. 2(a)) depicts a wrinkled membrane surface without distinct pinholes and cracks. The wrinkles on the surface of the RGO-MXene membrane are less than seen on the RGO membrane (Fig. 2(b)). The cross-sectional SEM images of the membranes (Figs. S6(a) and S6(b)) show that the RGO and RGO-MXene membranes have uniformly stacked lamellar structure. The XPS spectra show that the

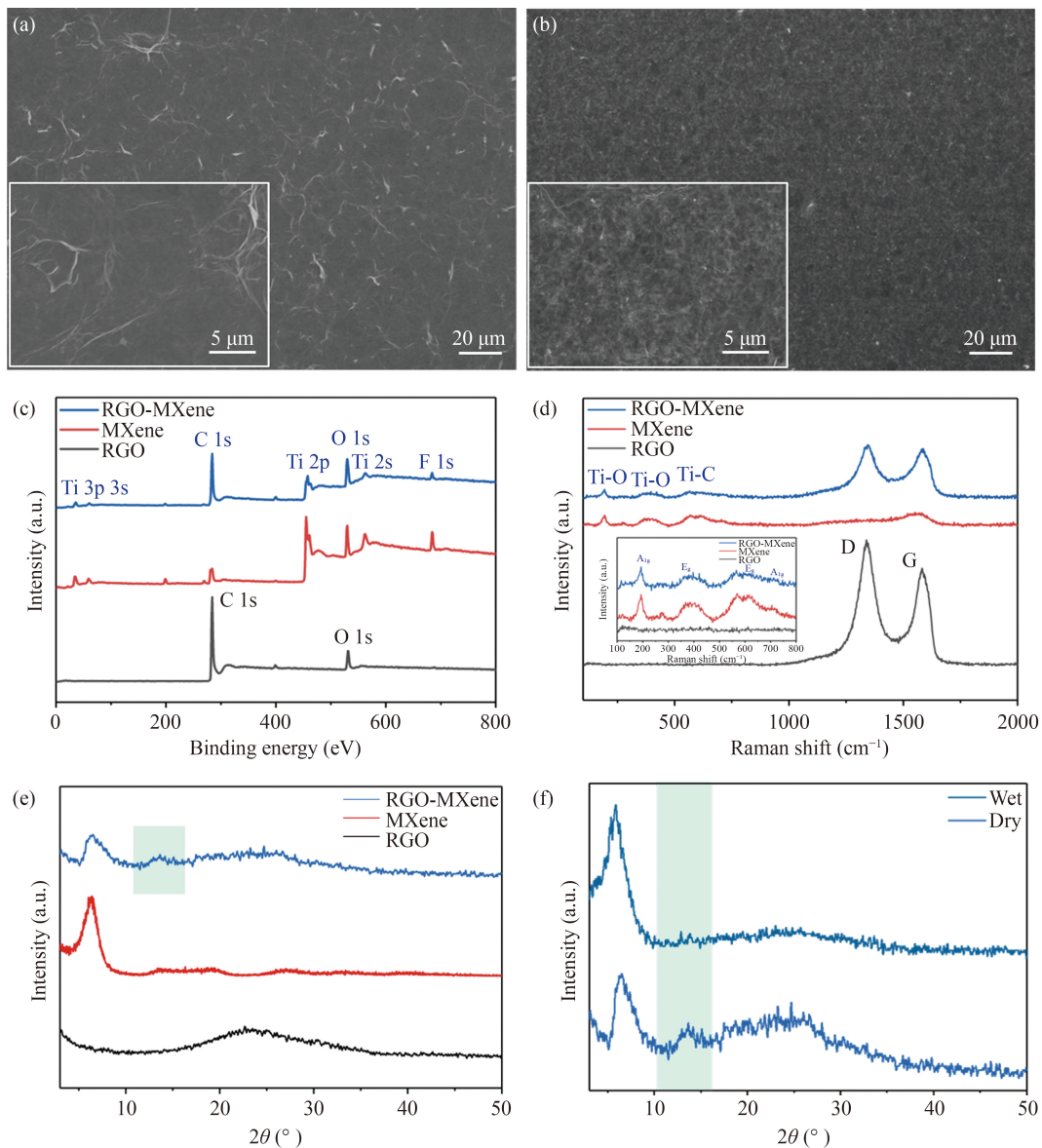


Fig. 2 SEM images of the surfaces of RGO (a) and RGO-MXene (b) membranes; (c) XPS spectra of RGO, MXene and RGO-MXene membranes; (d) Raman spectra of RGO, MXene and RGO-MXene membranes (inset: amplified Raman spectra of RGO, MXene and RGO-MXene membranes in the range of 100–800 cm^{-1}); (e) XRD patterns of RGO, MXene and RGO-MXene membranes; (f) XRD patterns of RGO-MXene membranes at wet and dry states.

main elements in MXene are Ti, C, O and F, and the characteristic peaks of Ti and F appear in the spectrum of the RGO-MXene membrane (Fig. 2(c)). The distribution of Ti seen in the cross-section of the RGO-MXene membrane shows that the MXene nanosheets are uniformly intercalated in the RGO nanosheets (Fig. S7). In the Raman spectrum of the RGO-MXene membrane (Fig. 2(d)), the peaks located at 194 and 719 cm^{-1} are assigned to A_{1g} vibrations of Ti and C atoms, and those located at 274, 367 and 624 cm^{-1} are attributed to the E_g group vibrations (Li et al., 2020), further indicating that MXene nanosheets are intercalated into the RGO-MXene membrane. The I_D/I_G value of the RGO membrane is 1.3, which is higher than that of the RGO-MXene membrane (~1.0), suggesting that the RGO-MXene membrane has fewer defects than the RGO membrane.

The interlayer spacings of RGO-MXene membranes were characterized by XRD. The pattern of the RGO membrane shows a diffraction peak at 23.4°, whereas that of the MXene membrane is located at 6.3° (Fig. 2(e)). For the RGO-MXene membrane, a new peak appears at 13.6°, which could be attributed to the interlayer spacing between the RGO and MXene nanosheets. Using the Bragg formula, the interlayer spacings of the RGO and RGO-MXene membranes are calculated as 0.38 and 0.65 nm, respectively. In addition, there is no obvious shift in the diffraction peak at 13.6° for the RGO-MXene membrane at the dry and wet states (Fig. 2(f)), indicating that the composite membrane could have good stability in water without exhibiting significant swelling.

3.3 Performances of RGO-MXene membranes

The effect of MXene on the permeability of the composite membrane was investigated by testing the pure water permeances of RGO-MXene membranes with different MXene mass percentages. As the MXene mass percentage increases from 0 to 70 wt.%, the pure water permeance significantly increases from 3.7 to 62.3 L/(m²·h·bar) (Fig. 3(a)), indicating that MXene intercalation can improve the pure water permeance of the RGO-MXene composite membrane. The relationship between the water permeance and interlayer spacing of a membrane can be described by the Hagen-Poiseuille equation (Nair et al., 2012) (detailed in Supporting Information, Eq. (S1)). When the interlayer spacing (δ) of the membrane increases from 0.38 to 0.65 nm, the water permeance (J) could increase by about 5 times. Notably, the pure water permeance of the RGO-MXene membrane is 16.8 times higher than that of the RGO membrane. This result indicates that the increased interlayer spacing is not the main reason for the improved water permeance. It can be speculated that the improved water permeance is related to the wettability of the RGO-MXene membranes, thus the water contact angles were tested. Fig. 3(b) shows that the RGO membrane has a water contact angle of 80.1°,

compared with 42.3° for the RM-70 membrane, indicating that the increase in the MXene mass percentage improves the hydrophilicity of the membrane. The zeta potential of the composite membranes is changed from -20.3 mV for the RGO membrane to -36.2 mV for the RM-70 membrane (Fig. S8), suggesting an increase in the surface functional groups of the composite membranes. The above results indicate that the intercalation of MXene enhances the wettability of the composite membrane, resulting in increased affinity between water molecules and the entrance of the membrane channels (Velioglu et al., 2018). This could allow water to enter the membrane channels easily, thereby increasing pure water permeance.

To further understand the water transport phenomenon, the movements of water molecules into two channels constructed by RGO-RGO and RGO-MXene nanosheets were investigated by molecular dynamics simulations (Figs. 3(c) and 3(d)). As shown in Fig. 3(e), the number of water molecules in the RGO-RGO channel reaches a constant value of about 129 when the time exceeds 41 ps, which is less than the constant value of about 187 in the RGO-MXene channel when the time exceeds 15 ps. Moreover, water molecules enter the RGO-MXene channel at higher rate of 12.5 ps⁻¹ than the RGO-RGO channel (3.1 ps⁻¹) (Fig. 3(f)). Fig. 3(g) shows that the interaction energy between water molecules and the RGO-MXene channel is 3505.2 kcal/mol, which is 6.5 times higher than that for the RGO-RGO channel (541.3 kcal/mol). This suggests that the intercalation of MXene enhances the interaction between water molecules and the membrane channel. Therefore, more water molecules are accelerated into the channel, which is conducive to rapid water transport for high water permeance.

Dye molecules of different sizes and charges are often used as target pollutants to investigate the rejection performance of nanofiltration membranes. Orange G (OG) with two negative charges is one of the most commonly used azo dyes (Ashok Kumar et al., 2019). Here, the effects of the mass percentage of MXene on the rejection performances of the composite membranes were investigated using negatively charged OG as a model pollutant. Fig. 3(h) shows that the permeant flux increases from 1.8 L/(m²·h·bar) for RGO membrane to 6.3 L/(m²·h·bar) for RM-30 membrane, while the OG rejection rate shows an inappreciable decrease from 88.8% to 88.0%. With a further increase in MXene mass percentage to 70 wt.%, the permeate flux of the membrane increases to 29.9 L/(m²·h·bar), whereas the OG rejection rate is declined to 27.7%. The results suggest that the RGO-MXene membrane exhibits a trade-off relationship between water permeance and dye rejection rate.

The rejection of charged dye by the RGO-MXene membrane is dependent on size sieving effect and electrostatic interactions between the membrane and charged dye. The RGO-MXene membrane has a conductivity of ~1100 S/m, and so to overcome the trade-off between

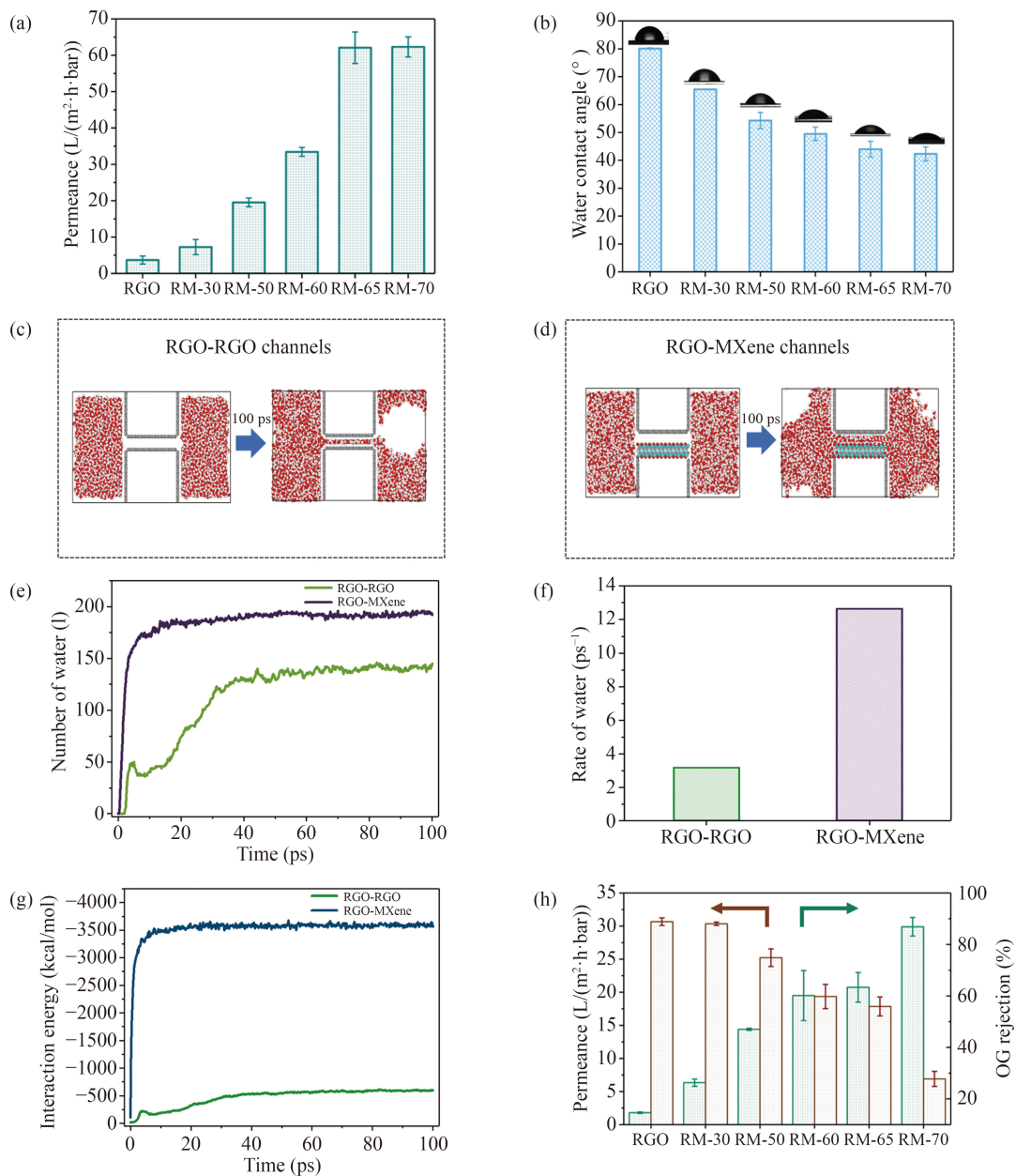


Fig. 3 Pure water permeances (a) and water contact angles (b) of RGO, RM-30, RM-50, RM-60, RM-65 and RM-70 membranes; (c, d) Molecular dynamics simulations of water molecules through RGO-RGO channels and RGO-MXene channels: Snapshots of water molecules in the two channels when the simulation time is 0 ps and 100 ps in the simulation system; (e) The number of water molecules in the RGO-RGO and RGO-MXene channels as the function of time; (f) The rates of water molecules entering RGO-RGO and RGO-MXene channels; (g) The interaction energies between water molecules and the RGO-RGO and RGO-MXene channels as the function of time; (h) Permeate fluxes and OG rejection rates of RGO, RM-30, RM-50, RM-60, RM-65 and RM-70 membranes (OG concentration: 20 mg/L; pressure: 1 bar).

flux and rejection, an electro-assistance strategy was adopted to enhance the electrostatic interactions and further improve the rejection performance. The membrane cathode potential and cyclic voltammetry (CV) curves are displayed in Fig. S9. When a voltage applied to the electric-assisted membrane system exceeds 2.0 V (corresponding to the membrane potential of -0.8 V vs. Ag/AgCl), a significant increase in electric current can be observed

from the CV curve, which could be ascribed to the noticeable hydrogen evolution reaction. Thus, the effects of electro-assistance on membrane performance are investigated at voltages ranging from 0 to 2.0 V.

The OG rejection performances of the RGO, RM-30, RM-50, RM-60, RM-65 and RM-70 membranes were tested at 2.0 V. Figs. 4(a) and 4(b) show the permeate fluxes and OG rejection rates of the membranes at 0 V

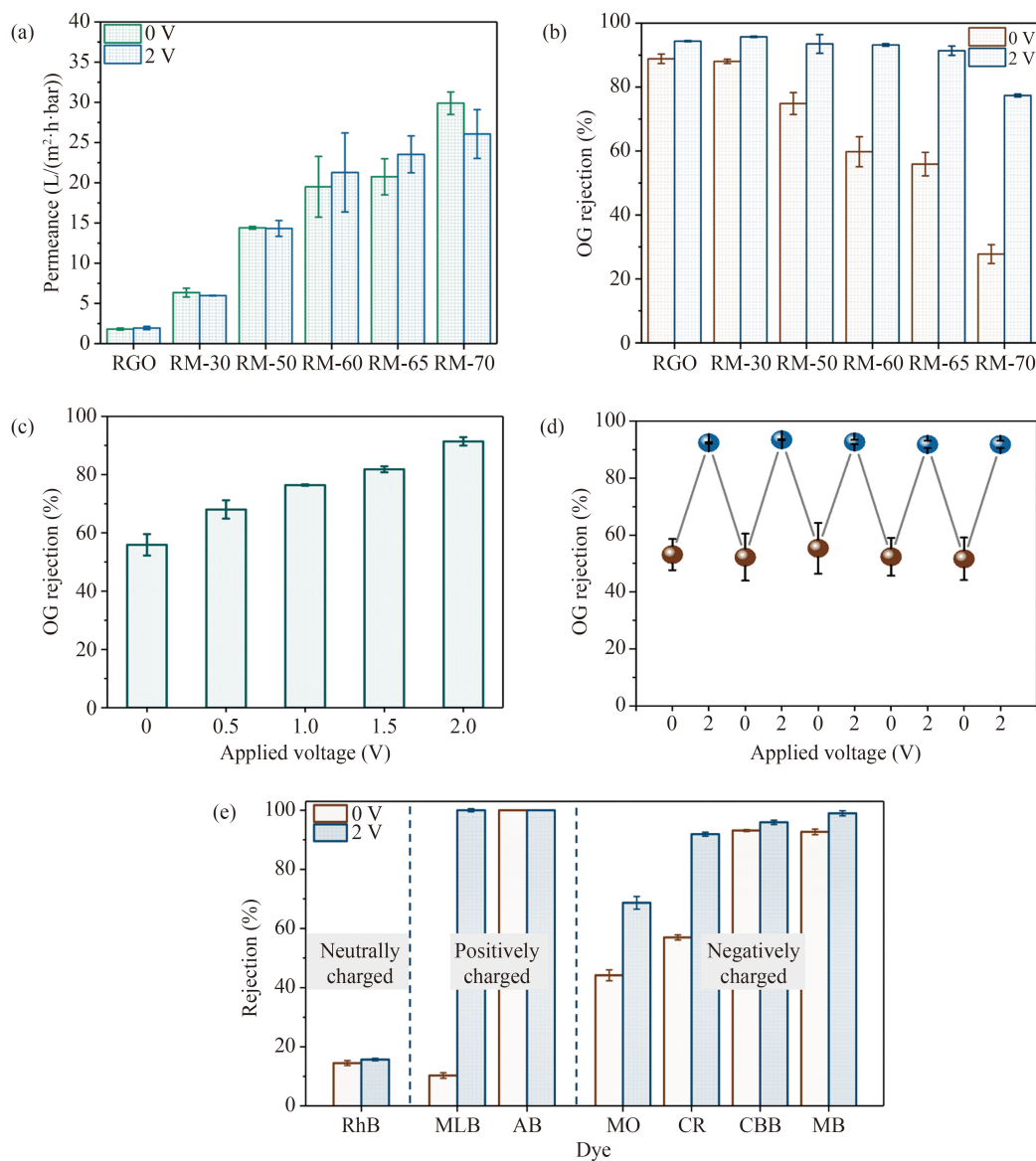


Fig. 4 (a) Permeate fluxes and (b) OG rejection rates of RGO, RM-30, RM-50, RM-60, RM-65 and RM-70 membranes under 0 V and 2.0 V; (c) OG rejection rates of RM-65 membrane under different voltages; (d) OG rejection rates of RM-65 membrane without and with electro-assistance for 5 cycles; (e) Rejection rates of RM-65 membrane for RhB (neutrally charged), MLB and AB (positively charged), MO, CR, CBB and MB (negatively charged) under 0 V and 2.0 V (dye concentration: 20 mg/L; pressure: 1 bar).

and 2.0 V, respectively. It can be seen that the applied voltage has no noticeable effect on the permeate flux. Notably, the OG rejection rate can be significantly improved after applying voltage, which indicates that electro-assistance can improve membrane rejection while maintaining high water permeability. For the membranes with the mass percentage of MXene ranging from 0 to 65 wt.%, OG rejection rate can be maintained at more than 90% under the electro-assistance of 2.0 V, with only a narrow range of variation changed from 94.4% for the RGO membrane to 91.4% for the RM-65 membrane. In comparison, when MXene mass percentage reaches 70 wt.%, the OG rejection rate decreases to 77.4%. Considering both permeate flux and rejection rate, the

RM-65 membrane is selected as the optimal membrane and used in subsequent experimental tests.

The OG rejection rates of the RM-65 membrane were evaluated at 0, 0.5, 1.0, 1.5 and 2.0 V. Fig. 4(c) shows that the OG rejection rate gradually improves with increasing voltage, confirmed by the fading the permeate solutions (Fig. S10(a)). The above results demonstrate that electro-assistance plays a significant role in improving rejection rate. The UV absorption spectrum of OG permeate solution shows that the absorbance at 478 nm decreases and no other absorption peak appears (Fig. S10(b)), indicating that the increased OG rejection is attributed to the enhanced electrostatic repulsion under electro-assistance. The recyclability of the electro-assisted membrane was

further tested by switching between electricity-off and electricity-on operations. After five electricity-off and electricity-on cycles (Fig. 4(d)), the OG rejection rate of the RM-65 membrane is maintained at ~52% at 0 V and ~92% at 2.0 V, indicating that electro-assisted RGO-MXene membrane has good recyclability.

The rejection performance of the RM-65 membrane under electro-assistance was further evaluated using other dyes with various sizes and charges, including RhB, MLB, AB, MO, CR, CBB and MB (Fig. 4(e)). For the neutrally charged RhB, the membrane shows a rejection rate of 15.3% at 0 V, and it only changes to 16.1% at 2.0 V, indicating that electro-assistance has a negligible effect on the rejection of neutrally charged dye. By contrast, the rejection rate of positively charged MLB is improved from 35.5% to 97.8% as the voltage increases from 0 to 2.0 V, with a particularly significant increase from 1.0 to 1.5 V (Fig. S11). The electrochemical reduction potential of MLB is about -0.2 V (Zhang et al., 2008). The cathodic potential of the membrane is about -0.4 V under an applied voltage of 1.5 V, which exceeds the reduction potential of MLB. Therefore, it is speculated that an electrochemical reduction reaction may have occurred in the system. The rejection rate of positively charged AB can be maintained at 100% after changing the voltage from 0 to 2.0 V, because the molecule size of AB (2.5 nm × 2.3 nm) is larger than the membrane interlayer spacing (Wu et al., 2021).

The molecular sizes of the four negatively charged dyes are: MO < CR < CBB ≈ MB (Wu et al., 2021). For MO, the membrane shows a low rejection rate of 44.1%, which may be because of its smaller molecular width (0.4 nm) compared with the membrane interlayer spacing (0.65 nm). For dyes with larger molecular size, the membrane shows an improved rejection rates, exceeding 92.7% for MB and CBB dyes. The above results indicate that the rejection rates of negatively charged dyes by the membrane are positively correlated with the molecular size of dyes. All of the rejection rates for these dyes are improved after applying the voltage of 2.0 V. The membrane surface is negatively charged, and the membrane acts as the cathode in the electro-assisted system, thus, electrical assistance could enhance the electrostatic repulsion between the membrane and negatively charged dyes. To analyze the underlying mechanism, the dye permeate solutions through the membrane at 2.0 V were analyzed by UV-visible absorption spectrometer (Fig. S12). The results show that there are no new products in the permeate solutions of CR, CBB or MB (Figs. S12(a)–S12(c)), which implies that the dye rejections are not ascribed to the dye degradation reactions. Because both the membrane surface and these dyes are negatively charged, electrostatic repulsion between the membrane and negatively charged dyes can be improved by enhanced surface charge density of the membrane under electro-assistance (Zhang et al., 2019). Thus, it is concluded that enhanced

electrostatic repulsion mainly contributes to the increased rejection rates of these dyes (CR, CBB and MB). The MO permeate solution shows a new UV absorption peak (Fig. S12(d)), indicating that electrochemical degradation occurs in the system. This result implies that the removal of MO is assisted by electrochemical reduction in addition to electrostatic repulsion at 2.0 V. Compared with results reported previously in the literatures (Table 1), the RGO-MXene membrane has considerably higher water permeance and comparable dye rejection rates. Taking account of both water flux and rejection rate, the RGO-MXene membrane exhibits superior performance compared to most other reported membranes.

4 Conclusions

In this work, electroconductive RGO-MXene membranes are prepared by intercalating MXene into RGO membranes. The wettability of the membrane is regulated by tuning the mass percentage of MXene in the composite membrane. The pure water permeance of the RGO-MXene membrane is about 16.8 times higher than that of the RGO membrane. Wettability characteristics and molecular dynamics simulations reveal that membrane wettability and the rate of water molecules entering the membrane channels are important factors for improving water flux. In addition, the RGO-MXene membrane exhibits improved rejection rates for charged dyes under electro-assistance. This work is expected to provide a new perspective for future research on the construction of novel membrane channel structures with high water transport and molecule rejection.

Table 1 Filtration performance of RM-65 membrane compared with previous membranes

Membrane	Water flux (L/(m ² ·h·bar))	Dye concentration (mg/L)	Dye rejection rate (%)	Reference
GO/Co(OH) ₂	2.8	20	CR, CBB > 98.0	Dong et al., 2020b
nano-TiO ₂ /PVA	5.0	50	MLB, 92.0MO, 52.1CR, 94.0	Li et al., 2014
GO/NH ₂ -Fe ₃ O ₄	15.6	100	MLB, 70.0MO, 75.0CR, 94.0	Dong et al., 2020a
TFC-2	17.0	100	CR, 85.0	Ounifi et al., 2022
PEI-g-GA@HPAN	25.5	100	CR, 97.1MB, 97.3	Zhao and Wang, 2017
c-CNT@GO	26.3	100	CR, 98.7MB, 94.1	Huang et al., 2021
RGO-MXene	62.1	20	MLB, 97.8MO, 68.7CR, 92.5MB, 99.0	This work

Acknowledgements This research was supported by the National Key Research and Development Program of China (No. 2020YFA0211001), the National Natural Science Foundation of China (Nos. 21976024 and 22106017), and the Programme of Introducing Talents of Discipline to Universities (China) (B13012).

Electronic Supplementary Material Supplementary material is available in the online version of this article at <https://doi.org/10.1007/s11783-023-1601-8> and is accessible for authorized users.

References

- Abaie E, Xu L, Shen Y X (2021). Bioinspired and biomimetic membranes for water purification and chemical separation: a review. *Frontiers of Environmental Science & Engineering*, 15(6): 124
- Abraham J, Vasu K S, Williams C D, Gopinadhan K, Su Y, Cherian C T, Dix J, Prestat E, Haigh S J, Grigorieva I V, Carbone P, Geim A K, Nair R R (2017). Tunable sieving of ions using graphene oxide membranes. *Nature Nanotechnology*, 12(6): 546–550
- Ashok Kumar S, Srinivasan G, Govindaradjane S (2019). Development of a new blended polyethersulfone membrane for dye removal from synthetic wastewater. *Environmental Nanotechnology, Monitoring & Management*, 12: 100238
- Dong L L, Li M H, Zhang S, Si X J, Bai Y X, Zhang C F (2020a). $\text{NH}_2\text{-Fe}_3\text{O}_4$ -regulated graphene oxide membranes with well-defined laminar nanochannels for desalination of dye solutions. *Desalination*, 476: 114227
- Dong Y P, Lin C, Gao S J, Manoranjan N, Li W X, Fang W X, Jin J (2020b). Single-layered GO/LDH hybrid nanoporous membranes with improved stability for salt and organic molecules rejection. *Journal of Membrane Science*, 607: 118184
- Fan X T, Cai C B, Gao J, Han X L, Li J D (2020). Hydrothermal reduced graphene oxide membranes for dyes removing. *Separation and Purification Technology*, 241: 116730
- Huang L, Huang S, Venna S R, Lin H (2018). Rightsizing nanochannels in reduced graphene oxide membranes by solvating for dye desalination. *Environmental Science & Technology*, 52(21): 12649–12655
- Huang L L, Li Z Y, Luo Y, Zhang N, Qi W X, Jiang E, Bao J J, Zhang X P, Zheng W J, An B G, He G H (2021). Low-pressure loose GO composite membrane intercalated by CNT for effective dye/salt separation. *Separation and Purification Technology*, 256: 117839
- Li W, Li X F, Chang W, Wu J, Liu P F, Wang J J, Yao X, Yu Z Z (2020). Vertically aligned reduced graphene oxide/ $\text{Ti}_3\text{C}_2\text{T}_x$ MXene hybrid hydrogel for highly efficient solar steam generation. *Nano Research*, 13(11): 3048–3056
- Li X P, Chen Y B, Hu X Y, Zhang Y F, Hu L J (2014). Desalination of dye solution utilizing PVA/PVDF hollow fiber composite membrane modified with TiO_2 nanoparticles. *Journal of Membrane Science*, 471: 118–129
- Li Z K, Liu Y C, Li L B, Wei Y Y, Caro J, Wang H (2019). Ultra-thin titanium carbide (MXene) sheet membranes for high-efficient oil/water emulsions separation. *Journal of Membrane Science*, 592: 117361
- Lian B, De Luca S, You Y, Alwarappan S, Yoshimura M, Sahajwalla V, Smith S C, Leslie G, Joshi R K (2018). Extraordinary water adsorption characteristics of graphene oxide. *Chemical Science*, 9(22): 5106–5111
- Liu Q, Chen M Q, Mao Y Y, Liu G P (2021). Theoretical study on Janus graphene oxide membrane for water transport. *Frontiers of Chemical Science and Engineering*, 15(4): 913–921
- Liu T, Liu X Y, Graham N, Yu W Z, Sun K N (2020). Two-dimensional MXene incorporated graphene oxide composite membrane with enhanced water purification performance. *Journal of Membrane Science*, 593: 117431
- Ming X, Guo A K, Zhang Q, Guo Z Z, Yu F, Hou B F, Wang Y, Homewood K P, Wang X B (2020). 3D macroscopic graphene oxide/MXene architectures for multifunctional water purification. *Carbon*, 167: 285–295
- Naguib M, Kurtoglu M, Presser V, Lu J, Niu J, Heon M, Hultman L, Gogotsi Y, Barsoum M W (2011). Two-dimensional nanocrystals produced by exfoliation of Ti_3AlC_2 . *Advanced Materials*, 23(37): 4248–4253
- Nair R R, Wu H A, Jayaram P N, Grigorieva I V, Geim A K (2012). Unimpeded permeation of water through helium-leak-tight graphene-based membranes. *Science*, 335(6067): 442–444
- Ounifi I, Guesmi Y, Ursino C, Castro-Muñoz R, Agougui H, Jabli M, Hafiane A, Figoli A, Ferjani E (2022). Synthesis and characterization of a thin-film composite nanofiltration membrane based on polyamide-cellulose acetate: application for water purification. *Journal of Polymers and the Environment*, 30(2): 707–718
- Pandey R P, Rasheed P A, Gomez T, Azam R S, Mahmoud K A (2020). A fouling-resistant mixed-matrix nanofiltration membrane based on covalently cross-linked $\text{Ti}_3\text{C}_2\text{T}_x$ (MXene)/cellulose acetate. *Journal of Membrane Science*, 607: 118139
- Park S, An J, Jung I, Piner R D, An S J, Li X, Velamakanni A, Ruoff R S (2009). Colloidal suspensions of highly reduced graphene oxide in a wide variety of organic solvents. *Nano Letters*, 9(4): 1593–1597
- Sang X, Xie Y, Lin M W, Alhabeb M, Van Aken K L, Gogotsi Y, Kent P R C, Xiao K, Unocic R R (2016). Atomic defects in monolayer titanium carbide ($\text{Ti}_3\text{C}_2\text{T}_x$) MXene. *ACS Nano*, 10(10): 9193–9200
- Su Y, Kravets V G, Wong S L, Waters J, Geim A K, Nair R R (2014). Impermeable barrier films and protective coatings based on reduced graphene oxide. *Nature Communications*, 5(1): 4843
- Sun J Q, Hu C Z, Liu Z T, Liu H J, Qu J H (2019). Surface charge and hydrophilicity improvement of graphene membranes via modification of pore surface oxygen-containing groups to enhance permeability and selectivity. *Carbon*, 145: 140–148
- Velioğlu S, Han L, Chew J W (2018). Understanding membrane pore-wetting in the membrane distillation of oil emulsions via molecular dynamics simulations. *Journal of Membrane Science*, 551: 76–84
- Wang H, Gao B, Hou L A, Shon H K, Yue Q, Wang Z (2021). Fertilizer drawn forward osmosis as an alternative to 2nd pass seawater reverse osmosis: Estimation of boron removal and energy consumption. *Frontiers of Environmental Science & Engineering*, 15(6): 135
- Wei G L, Dong J, Bai J, Zhao Y S, Li Y (2019a). Structurally stable, antifouling, and easily renewable reduced graphene oxide membrane with a carbon nanotube protective layer. *Environmental Science & Technology*, 53(20): 11896–11903

- Wei G L, Zhao Y S, Dong J, Gao M, Li C (2020). Electrochemical cleaning of fouled laminar graphene membranes. *Environmental Science & Technology Letters*, 7(10): 773–778
- Wei S, Du L, Chen S, Yu H T, Quan X (2021). Electro-assisted CNTs/ceramic flat sheet ultrafiltration membrane for enhanced antifouling and separation performance. *Frontiers of Environmental Science & Engineering*, 15(1): 11
- Wei S C, Xie Y, Xing Y D, Wang L C, Ye H Q, Xiong X, Wang S, Han K (2019b). Two-dimensional graphene oxide/MXene composite lamellar membranes for efficient solvent permeation and molecular separation. *Journal of Membrane Science*, 582: 414–422
- Willcox J A, Kim H J (2017a). Molecular dynamics study of water flow across multiple layers of pristine, oxidized, and mixed regions of graphene oxide: effect of graphene oxide layer-to-layer distance. *Journal of Physical Chemistry C*, 121(42): 23659–23668
- Willcox J A L, Kim H J (2017b). Molecular dynamics study of water flow across multiple layers of pristine, oxidized, and mixed regions of graphene oxide. *ACS Nano*, 11(2): 2187–2193
- Wu Y, Fu C F, Huang Q, Zhang P, Cui P, Ran J, Yang J, Xu T (2021). 2D heterostructured nanofluidic channels for enhanced desalination performance of graphene oxide membranes. *ACS Nano*, 15(4): 7586–7595
- Xu W L, Fang C, Zhou F, Song Z, Liu Q, Qiao R, Yu M (2017). Self-assembly: a facile way of forming ultrathin, high-performance graphene oxide membranes for water purification. *Nano Letters*, 17(5): 2928–2933
- Xu W L, Zhou F L, Yu M (2018). Tuning water nanofiltration performance of few-layered, reduced graphene oxide membranes by oxygen plasma. *Industrial & Engineering Chemistry Research*, 57(47): 16103–16109
- Yi G, Chen S, Quan X, Wei G L, Fan X F, Yu H T (2018). Enhanced separation performance of carbon nanotube-polyvinyl alcohol composite membranes for emulsified oily wastewater treatment under electrical assistance. *Separation and Purification Technology*, 197: 107–115
- Zhang H, Quan X, Fan X, Yi G, Chen S, Yu H, Chen Y (2019). Improving ion rejection of conductive nanofiltration membrane through electrically enhanced surface charge density. *Environmental Science & Technology*, 53(2): 868–877
- Zhang J D, Zheng Y Q, Jiang G D, Yang C Z, Oyama M (2008). Electrocatalytic evaluation of liquid phase deposited methylene blue/TiO₂ hybrid films. *Electrochemistry Communications*, 10(7): 1038–1040
- Zhao S, Wang Z (2017). A loose nano-filtration membrane prepared by coating HPAN UF membrane with modified PEI for dye reuse and desalination. *Journal of Membrane Science*, 524: 214–224